# Lawrence Berkeley National Laboratory
## LBL Publications

**Title**

Pore-Scale Modeling of Reactive Transport with Coupled Mineral Dissolution and Precipitation

**Permalink**

https://escholarship.org/uc/item/0dc1n4pj

**Journal**

Water Resources Research, 60(6)

**ISSN**

**Authors**

Wang, Ziyan

Hu, Mengsu

Steefel, Carl

**Publication Date**

2024-06-01

**DOI**

**Copyright Information**

Peer reviewed

**Correspondence to:**
Z. Wang,
ziyanw@lbl.gov

# Pore-Scale Modeling of Reactive Transport with Coupled Mineral Dissolution and Precipitation

**Ziyan Wang[1]** , **Mengsu Hu[1]** , and **Carl Steefel[1]**

[1]Energy Geosciences Division, Lawrence Berkeley National Laboratory, Berkeley, CA, USA

**Abstract** We present a new pore-scale model for multicomponent advective-diffusive transport with coupled mineral dissolution and precipitation. Both dissolution and precipitation are captured simultaneously by introducing a phase transformation vector field representing the direction and magnitude of the overall phase change. An effective viscosity model is adopted in simulating fluid flow during mineral dissolution-precipitation that can accurately capture the velocity field without introducing any empirical parameters. The proposed approach is validated against analytical solutions and interface tracking simulations in simplified structures. After validation, the proposed approach is employed in modeling realistic rocks where mineral dissolution and precipitation are dominant at different locations. We have identified three regimes for mineral dissolution-precipitation coupling: (a) compact dissolution-precipitation where dissolution is dominant near the inlet and precipitation is dominant near the outlet, (b) wormhole dissolution with clustered precipitation where dissolution generates wormholes in the main flow paths and precipitation clogs the secondary flow paths, and (c) dissolution dominant where all solid grains are gradually dissolved. In the three regimes, the proposed approach provides reliable porosity-permeability relationships that cannot be described well by traditional macroscale models. We find that the permeability can increase while the overall porosity decreases when the main flow paths are expanded by dissolution and adjacent pore spaces are clogged by precipitation.

## 1. Introduction

Coupled mineral dissolution-precipitation during reactive transport is important in many applications with water-rock interaction such as geological $CO_2$ sequestration (Kampman et al., 2014; Sabo & Beckingham, 2021; R. Xu et al., 2017), enhanced geothermal systems (Rabemanana et al., 2005), and contamination treatment in groundwater resources (Burns & Klingensmith, 2006). Mineral dissolution and precipitation occur because the local fluid is chemically undersaturated or supersaturated with respect to equilibrium. This can be caused by the change of solubility depending on temperature (Hu & Rutqvist, 2020; Steefel & Lasaga, 1990) and pressure (i.e., pressure solution, Gratier et al., 2009; Yasuhara et al., 2005), or by introducing additional chemical species, for example, acid injection (Singurindy & Berkowitz, 2005; Xie et al., 2015). In porous media, mineral dissolution-precipitation typically alters the pore space geometry, thus affecting the pathways for fluid flow and solute transport (Ling et al., 2022; Steefel et al., 2013; Steefel & Hu, 2022). Due to the complex geometric features and the coupling of multiple physical processes, it is challenging to describe the impact of mineral dissolution-precipitation on flow and transport properties of a porous medium. One common scenario is that the dissolution of one phase drives the precipitation of another, where dissolution and precipitation can be dominant at different locations, for example, the reaction of calcite with acidic, sulfate-bearing solutions to form gypsum (Singurindy & Berkowitz, 2005; Xie et al., 2015). Such examples are the primary focus of this paper, while we can also employ the proposed model in scenarios where mineral dissolution and precipitation are driven by temperature or pressure differences.

Macroscale models describe a porous structure as an effective medium with evolving porosity and permeability during mineral dissolution-precipitation (Borgia et al., 2012; Deng et al., 2016). Typically, the porosity can be updated based on the amount of minerals being dissolved or precipitated. The permeability, on the other hand, is much more difficult to evaluate. For example, previous studies have reported that the rock permeability can decrease while the porosity increases during simultaneous mineral dissolution and precipitation (Sabo & Beckingham, 2021). Traditional permeability models, such as the Carman-Kozeny equation (Carman, 1997), may not be applicable in this case as the permeability-porosity relationship can vary with the relative significance between dissolution and precipitation. Therefore, pore-scale models may offer an improved understanding as they

can explicitly resolve the evolving pore space geometry as a result of coupled fluid flow, solute transport, and mineral reactions.

Many pore-scale models have been developed to describe the moving interface during mineral reactions (Molins et al., 2021). They can be divided into two categories: interface tracking and interface capturing approaches (Ge et al., 2012). In interface tracking approaches, a fluid-solid interface is treated as a computational boundary and boundary-fitted mesh is employed to follow the interface movement (Juric & Tryggvason, 1996; Starchenko et al., 2016; Starchenko & Ladd, 2018). One example is the Arbitrary-Lagrangian-Eulerian method, which has been adopted to model fracture and grain dissolution (Oltean et al., 2013; Starchenko et al., 2016). For complex porous structures, however, adapting the mesh to account for moving interfaces can be challenging, especially when the topology of the structure changes. In interface capturing approaches, an indicator function is defined in both fluid and solid phases to represent the interface location. Commonly adopted indicator functions include the level-set function (X. Li et al., 2010; Ray et al., 2019), the phase fraction function (e.g., in the micro-continuum method, Soulaine & Tchelepi, 2016; Soulaine et al., 2017; Yang et al., 2021 and the phase field method, Z. Xu & Meakin, 2008; Z. Xu et al., 2012), and the binarize function that distinguishes fluid and solid (e.g., in the lattice Boltzmann method, Kang et al., 2003; Huber et al., 2014; Poonoosamy et al., 2019). Hybrid models are also developed to take advantage of different methods, for example, dissolution modeling with lattice Boltzmann, finite volume and surface rescaling methods (Gray & Boek, 2016; Gray et al., 2016, 2018, 2021). These methods generally work on fixed meshes, avoiding costly mesh updates that may perform better for modeling complex porous structures.

The pore-scale models are usually developed with a focus on either dissolution or precipitation, although mineral reactions often involve both coupled together (Li et al., 2017; Maher et al., 2009; Steefel & Van Cappellen, 1990; Steefel & Yang, 2021). In the literature, the pore-scale models that can capture dissolution and precipitation simultaneously are much more limited. The lattice Boltzmann method has been employed to solve the coupled dissolution-precipitation problems (Chen et al., 2014; Jiang et al., 2021). In the lattice Boltzmann method, each computational cell represents pure fluid or solid, and the switch of the cell state represents dissolution or precipitation. One challenge is to design the criteria when the cell state switches, as there is no a priori rule, and the criteria can significantly affect the dissolution-precipitation pattern (Chen et al., 2014). Recently, Deng et al. (2022) developed a micro-continuum model for mineral growth with co-dissolution, while the porous structure is simplified as a slit and mineral precipitation is dominant over dissolution. A fully coupled dissolution-precipitation model in complex porous structures is still desired.

In this study, we have developed a new pore-scale model for coupled mineral dissolution and precipitation in which the phase fraction field is adopted to capture the fluid-solid interface movement. A major challenge is to properly describe the interface growing and retreating during the precipitation and dissolution of different minerals, for example, the dissolution of calcite and the precipitation of gypsum at different locations (Figure 1). We introduce a phase transformation vector field to represent the direction and magnitude of the dissolution-precipitation process and update the phase fraction field accordingly. In addition, an effective viscosity model is adopted to immobilize fluid flow at fluid-solid interfaces, which captures the velocity field accurately without introducing any empirical parameters. For the case of coupled dissolution and precipitation, we investigate the resulting porosity-permeability relationships, which have not been comprehensively described by macroscale models.

The manuscript is organized as follows. Section 2 presents the physical model of the reactive system we consider. Section 3 describes the proposed computational model, including the interface capturing approach and the associated numerical methods. In Section 4, the model is validated against analytical solutions and interface tracking simulations in simplified structures, and then applied in realistic rocks. Section 5 contains the discussion of the results and the conclusions.

## 2. Physical Model

We consider a reactive flow system with multiple reactive species. Fluid flow at the pore scale is governed by the Navier-Stokes equations for incompressible Newtonian fluid:

$$\nabla \cdot \mathbf{u} = 0 \,, \tag{1a}$$
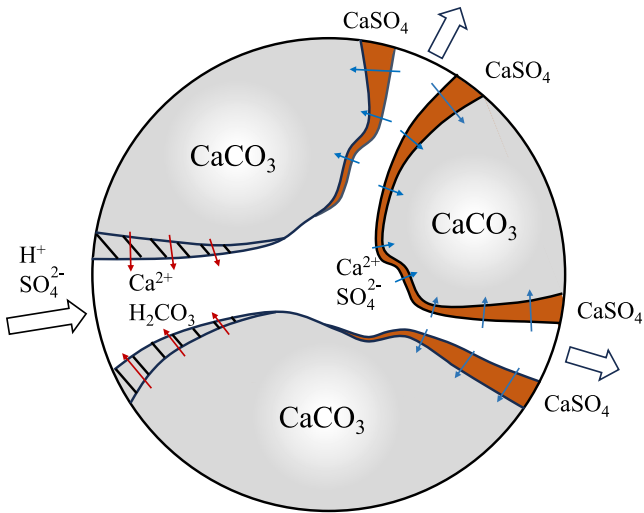
**Figure 1.** A schematic representation of coupled calcite dissolution and gypsum precipitation at different locations in a granular porous structure. In some case, the secondary mineral may not completely cover the dissolving primary phase.

$$\rho_f \left[ \frac{\partial \mathbf{u}}{\partial t} + \nabla \cdot (\mathbf{uu}) \right] = -\nabla p + \nabla \cdot \left( \mu_f \nabla \mathbf{u} \right), \tag{1b}$$

where $\mathbf{u}\,(\mathbf{x},\, t) = (u\,(\mathbf{x},\, t),\, v(\mathbf{x},\, t),\, w\,(\mathbf{x},\, t))$, $p\,(\mathbf{x},\, t)$, $\rho_f$ and $\mu_f$ are the fluid's velocity, pressure, density, and dynamic viscosity, respectively. Here the fluid density $\rho_f$ is assumed to be constant and independent of the solute concentration. The transport of multiple solute components is described by the advection-diffusion equation:

$$\frac{\partial c_i}{\partial t} + \nabla \cdot (\mathbf{u}c_i) = \nabla \cdot (D_i \nabla c_i), \tag{2}$$

where $c_i$ is the concentration of solute component $i$ and $D_i$ is the corresponding diffusivity. We assume there are no homogeneous reactions (e.g., aqueous complexation) taking place in the fluid phase.

At fluid-solid interfaces, the solute or solutes undergoes a heterogeneous reaction that consists of mineral dissolution or precipitation. This is described by boundary conditions on the fluid-solid interfaces:

$$\mathbf{n} \cdot \left( -D_i \nabla c_i + \mathbf{u}|_\Gamma c_i - \mathbf{U}_\Gamma c_i \right) = R_i, \tag{3a}$$

$$\mathbf{n} \cdot \mathbf{U}_\Gamma = Q, \tag{3b}$$

$$\mathbf{t} \cdot \mathbf{U}_\Gamma = 0, \tag{3c}$$

where $\mathbf{n}$ is the unit normal vector pointing from fluid to solid, $\mathbf{t}$ the unit tangent vector, $R_i$ the reaction rate (per area of mineral) for solute component $i$, and $Q$ is a signed dissolution-precipitation rate (per area of mineral), which is positive for dissolution and negative for precipitation. Explicit expressions for $R_i$ and $Q$ will be provided through a specific reactive system in Section 3. The velocity $\mathbf{u}|_\Gamma$ is the fluid velocity at the interface, while $\mathbf{U}_\Gamma$ is the interface velocity due to mineral dissolution-precipitation. We note that the two velocities $\mathbf{u}|_\Gamma$ and $\mathbf{U}_\Gamma$ should be distinguished (L. Li et al., 2021), and they both contribute to the mass conservation Equation 3a. The fluid velocity is non-zero when there is an overall volumetric change after mineral dissolution-precipitation. If the overall volume decreases, $\mathbf{n} \cdot \mathbf{u}|_\Gamma > 0$, and vice versa. The velocity $\mathbf{u}|_\Gamma$ is generally much less than the average flow velocity. For simplicity, we assume $\mathbf{u}|_\Gamma = 0$ in the computational modeling in Section 3.

## 3. Computational Model

Directly solving the governing equations in Section 2 requires explicitly tracking the location of fluid-solid interfaces and updating the mesh in the fluid domain to fit the moving boundary. This interface tracking approach works well for simple geometries. However, for complex porous structures, especially those that might involve multiple minerals, a more efficient approach is to introduce an indicator function, which implicitly captures the interface location. Because of the additional indicator function, a different set of governing equations is constructed that is designed to recover the solution of Equations 1–3. The model presented in this section is inspired by the micro-continuum approach (Soulaine et al., 2017; Soulaine & Tchelepi, 2016). However, instead of modeling the fluid-solid interface as a porous layer, we adopt effective properties in the interface. The two approaches are compared later in Section 4.2.

We employ the fluid phase fraction $\phi$ as the indicator function to distinguish fluid and solid phases, where $\phi = 0$ and $\phi = 1$ indicate pure solid and fluid, respectively. The interface is modeled as a smooth transitional region ($0 < \phi < 1$) that can spread over several grid cells. A single set of equations is solved in the entire computational domain, including both fluid and solid. For fluid flow, the momentum equation is obtained through volume averaging:

$$\frac{\rho_f}{\phi}\left[\frac{\partial \mathbf{u}}{\partial t} + \nabla \cdot \left(\frac{\mathbf{uu}}{\phi}\right)\right] = -\nabla p + \nabla \cdot \left(\mu_{eff}\nabla \mathbf{u}\right), \tag{4a}$$

$$\mu_{eff} = \frac{\mu_f}{\phi}, \tag{4b}$$

We assume the solid phase is not transported and thus $\mathbf{u} = \phi\mathbf{u}_f$, where $\mathbf{u}$ and $\mathbf{u}_f$ are the superficial and intrinsic fluid velocity, respectively. To improve numerical stability, the phase fraction has a lower bound of $\phi = 1 \times 10^{-5}$ in the pure solid phase.

The multi-component solute transport with mineral reactions is described as follows (Deng et al., 2021, 2022; Soulaine et al., 2017, 2021; Yang et al., 2021):

$$\frac{\partial(\phi c_i)}{\partial t} + \nabla \cdot (\mathbf{u}c_i) = \nabla \cdot (\phi D_{i,eff}\nabla c_i) - r_i, \tag{5a}$$

$$D_{i,eff} = \phi D_i, \tag{5b}$$

$$r_i = R_i|\nabla\phi|. \tag{5c}$$

Since the fluid-solid interface is modeled as a smooth transitional region, the interfacial reaction rate $R_i$ in Equation 3a is transformed into a volumetric reaction rate $r_i$, which is non-zero only in the transitional region. Here $|\nabla\phi|$ represents the reactive interface area per unit volume in the smooth transitional region. For mineral dissolution and precipitation, we have (Soulaine et al., 2017; Soulaine & Tchelepi, 2016):

$$\frac{\partial\phi}{\partial t} = Q|\nabla\phi|. \tag{6}$$

Similar to Eq. (3), we neglect the fluid velocity on the interface, so $\nabla \cdot \mathbf{u} = 0$ is satisfied in the entire computational domain.

To explicitly express the reaction rate $R_i$ and the dissolution-precipitation rate $Q$, we consider a specific reactive system:

$$A(s) + 2B(aq) \rightarrow C(aq) + D(aq), \tag{7a}$$

$$C(aq) + E(aq) \rightarrow F(s). \tag{7b}$$

For example, the reactive system can represent calcite dissolution and gypsum precipitation (Figure 1):

$$CaCO_3(s) + 2H^+(aq) \rightarrow Ca^{2+}(aq) + H_2CO_3(aq), \tag{8a}$$

$$Ca^{2+}(aq) + SO_4^{2-}(aq) \rightarrow CaSO_4(s). \tag{8b}$$
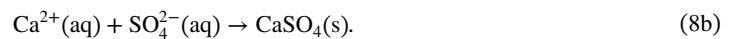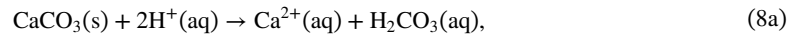
This system was considered in 2D reactive flow and transport simulations in Xie et al. (2015). In our case, we assume the reactive system is far from equilibrium, so the backward reactions are not considered. We focus on scenarios in which dissolution and precipitation are dominant at different locations (Figure 1). This generally occurs when the precipitation rate is lower or comparable to the dissolution rate. If precipitation is much faster than dissolution, the dissolved ions can precipitate instantaneously at the same location, for example, in celestite dissolution and barite precipitation (Deng et al., 2022). Since this has been investigated in the literature, our focus is the non-localized dissolution-precipitation coupling, which shows a more complicated behavior.

In the reactive system, we focus on the concentrations of three components that control the reaction rates ($i = 1,2,3$):

$$c_1 = c(B) \left(= \left[H^+\right]\right), \tag{9a}$$

$$c_2 = c(E) \left(= \left[SO_4^{2-}\right]\right), \tag{9b}$$

$$c_3 = c(C) \left(= \left[Ca^{2+}\right]\right). \tag{9c}$$

The interfacial and volumetric reaction rates in Equation 5 are:

$$R_1 = 2k_1 c_1, \qquad r_1 = 2k_1 c_1 |\nabla \phi|, \tag{10a}$$

$$R_2 = k_{23} c_2 c_3, \qquad r_2 = k_{23} c_2 c_3 |\nabla \phi|, \tag{10b}$$

$$R_3 = -k_1 c_1 + k_{23} c_2 c_3, \qquad r_3 = -k_1 c_1 |\nabla \phi| + k_{23} c_2 c_3 |\nabla \phi|, \tag{10c}$$

where $k_1$ and $k_{23}$ are reaction rate constants. Here the dissolution reaction (Equation 7a and Equation 8a) is assumed to be first order with respect to the component B ($H^+$), based on calcite dissolution experiments (Alkattan et al., 1998; Buhmann & Dreybrodt, 1985), and the precipitation reaction is second order overall, assuming elementary reaction kinetics. The mineral dissolution-precipitation process is described by:

$$\frac{\partial \phi}{\partial t} = k_1 V_1 c_1 |\nabla \phi| - k_{23} V_{23} c_2 c_3 |\nabla \phi|, \tag{11}$$

where $V_1$ and $V_{23}$ are the molar volume of the dissolved species A and the precipitated species F, respectively.

The governing equations in the computational model are discretized and solved by OpenFOAM (Weller et al., 1998), which is an open-source C++ library for computational fluid dynamics. A major challenge is to properly discretize Equation 11 so that the phase fraction $\phi$ is always bounded between 0 and 1 while the interface moves. For example, when mineral precipitation occurs, a pure fluid grid should be able to transform to a solid phase through mineral precipitation ($\frac{\partial \phi}{\partial t} < 0$), which indicates $|\nabla \phi| > 0$ in Equation 11. Mathematically, this condition is:

$$\exists \mathbf{x}, \phi(\mathbf{x}) = 1 \text{ and } |\nabla \phi| > 0. \tag{12}$$

On the other hand, when dissolution occurs, all pure fluid grid cells should remain in a fluid state ($\frac{\partial \phi}{\partial t} = 0$). According to Equation 11, this indicates:

$$\forall \mathbf{x} \text{ s.t. } \phi(\mathbf{x}) = 1, |\nabla \phi| = 0. \tag{13}$$
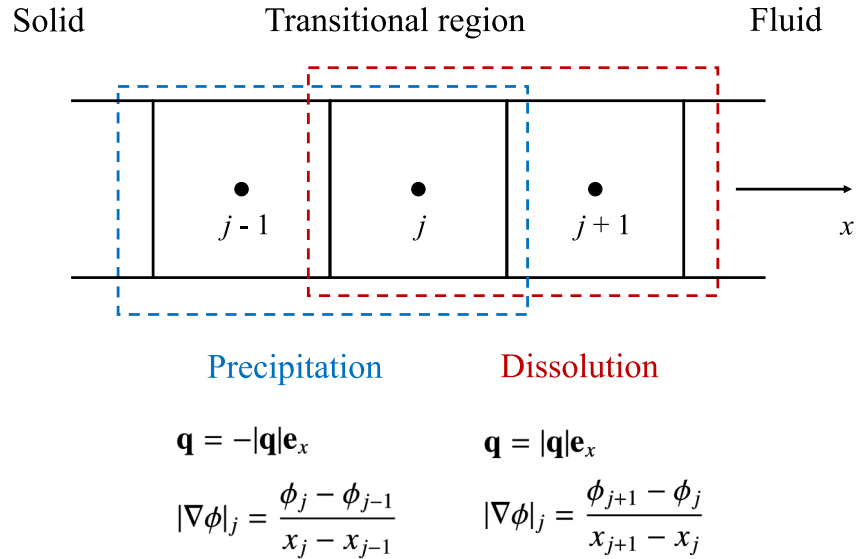
The two conditions (12) and (13) contradict each other, so $\nabla \phi$ needs to be computed based on the local state of dissolution or precipitation.

We define a phase transformation vector field:

$$\mathbf{q} = Q \nabla \phi = k_1 V_1 c_1 \nabla \phi - k_{23} V_{23} c_2 c_3 \nabla \phi. \tag{14}$$

The direction of $\mathbf{q}$ represents the direction of phase transformation: $\mathbf{q}$ pointing from solid to fluid indicates dissolution, and $\mathbf{q}$ pointing from fluid to solid indicates precipitation. The magnitude of $\mathbf{q}$ represents the volumetric rate of phase transformation. The term $\nabla \phi$ is computed as follows. First, we compute a temporary $\nabla \phi$ by traditional central differencing. Next, we substitute the temporary $\nabla \phi$ in Equation 14 to calculate $\mathbf{q}$. Finally, we compute $\nabla \phi$ again following the downwind differencing scheme, with the wind direction given by $\mathbf{q}$.

To demonstrate the algorithm, we construct a fluid-solid interface perpendicular to the $x$ axis, with solid in the $x^-$ direction and fluid in the $x^+$ direction. We consider three adjacent computational grid cells located at $x_{j-1} < x_j < x_{j+1}$ (Figure 2). Since the fluid is in the $x^+$ direction, the fluid phase fraction satisfies $\phi_{j-1} \leq \phi_j \leq \phi_{j+1}$. When mineral precipitation occurs, the phase transformation vector $\mathbf{q}$ points from fluid to solid, that is, in the $x^-$ direction. Following the downwind differencing scheme and applying Equation 6, we have:

Solid          Transitional region          Fluid



Precipitation          Dissolution

$$\mathbf{q} = -|\mathbf{q}|\mathbf{e}_x \qquad \mathbf{q} = |\mathbf{q}|\mathbf{e}_x$$

$$|\nabla\phi|_j = \frac{\phi_j - \phi_{j-1}}{x_j - x_{j-1}} \qquad |\nabla\phi|_j = \frac{\phi_{j+1} - \phi_j}{x_{j+1} - x_j}$$

**Figure 2.** Three adjacent grid cells in the transitional region between fluid and solid phases. The discretization of $|\nabla\phi|$ involves different grid connections for dissolution and precipitation, the choice of which depends on the direction of the phase transformation vector $\mathbf{q}$.

$$|\nabla\phi|_j = \frac{\phi_j - \phi_{j-1}}{x_j - x_{j-1}} \leq \frac{\phi_j}{x_j - x_{j-1}}, \tag{15a}$$

$$\frac{\partial\phi_j}{\partial t} = Q|\nabla\phi|_j \geq Q\frac{\phi_j}{x_j - x_{j-1}}. \tag{15b}$$

Since $Q$ is negative for mineral precipitation, Equation 15b ensures $\phi_j$ can only decrease and is always positive. Equation 15 also shows that $\phi_j$ can decrease from 1 as long as $\phi_{j-1} < \phi_j$. On the other hand, when mineral dissolution occurs, $\mathbf{q}$ is in the $x^+$ direction. Similarly, we have:

$$|\nabla\phi|_j = \frac{\phi_{j+1} - \phi_j}{x_{j+1} - x_j} \leq \frac{1 - \phi_j}{x_{j+1} - x_j}, \tag{16a}$$

$$\frac{\partial\phi_j}{\partial t} = Q|\nabla\phi|_j \leq Q\frac{1 - \phi_j}{x_{j+1} - x_j}. \tag{16b}$$

For mineral dissolution, $Q$ is positive, so Equation 16b guarantees that $\phi_j$ can only increase and is always bounded by 1. In conclusion, the phase transformation vector field $\mathbf{q}$ allows us to properly discretize the term $\nabla\phi$, so that $\phi$ is always bounded between 0 and 1 for both dissolution and precipitation scenarios.

For two-dimensional and three-dimensional problems, the discretization of $\nabla\phi$ follows the same downwind differencing scheme, with the wind direction given by $\mathbf{q}$. As an example, we consider a grid cell $(i,j)$ in a two-dimensional system where $\phi_{i,j-1} \leq \phi_{i,j} \leq \phi_{i,j+1}$ and $\phi_{i-1,j} \leq \phi_{i,j} \leq \phi_{i+1,j}$ (this can be modified following the interface direction). For mineral precipitation, we have:

$$(\nabla\phi)_{i,j} = \left(\frac{\phi_{i,j} - \phi_{i,j-1}}{x_{i,j} - x_{i,j-1}}, \frac{\phi_{i,j} - \phi_{i-1,j}}{x_{i,j} - x_{i-1,j}}\right). \tag{17}$$

For mineral dissolution, we have:

$$(\nabla\phi)_{i,j} = \left(\frac{\phi_{i,j+1} - \phi_{i,j}}{x_{i,j+1} - x_{i,j}}, \frac{\phi_{i+1,j} - \phi_{i,j}}{x_{i+1,j} - x_{i,j}}\right). \tag{18}$$
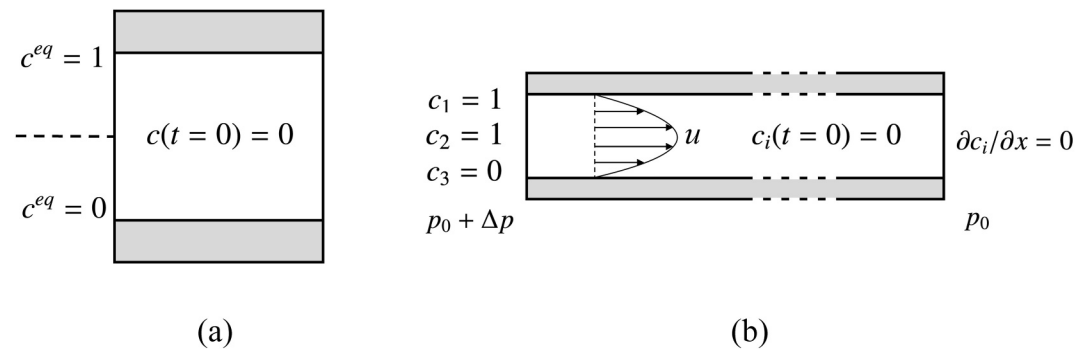
**Figure 3.** A schematic representation of the mineral dissolution-precipitation systems for model validation, where the white region represents the fluid and the gray region represents the solid at the initial state: (a) one-component diffusion-reaction problem in Section 4.1; (b) multicomponent reactive flow problem in Section 4.2, where the dashed lines indicate that the channel is much longer than shown here.

## 4. Results

To validate the model, we first consider a one-component diffusion-reaction problem, where analytical solutions exist for comparison (Section 4.1). Next, a multi-component reactive flow problem is solved, in which the proposed model is compared with a reference interface tracking approach (Section 4.2). Finally, the proposed model is applied in a realistic rock structure, where different dissolution-precipitation patterns are identified (Section 4.3).

### 4.1. Model Validation Against Analytical Solutions

To validate the computational model in Section 3, we start by considering a one-component diffusion-reaction system with coupled dissolution and precipitation. The reaction rate in Equation 5 and the dissolution-precipitation Equation 6 are explicitly expressed as:

$$r = k(c - c^{eq})|\nabla\phi|, \tag{19a}$$

$$\frac{\partial\phi}{\partial t} = -k(c - c^{eq})\,V|\nabla\phi|, \tag{19b}$$

where $c^{eq}$ is an equilibrium concentration which will be given in Equation 20. For simplicity, we investigate a one-dimensional problem, in which a fluid domain is located between two solid domains at the top and bottom (Figure 3a). The top half of the domain is set to have a higher $c^{eq}$ than the bottom half, for example, due to a temperature difference:

$$c^{eq}(y) = 1 \qquad y \in [0, H/2], \tag{20a}$$

$$c^{eq}(y) = 0 \qquad y \in [-H/2, 0), \tag{20b}$$

where $H$ is the domain height. Because of the different equilibrium concentration, the mineral gradually dissolves at the top fluid-solid interface and then precipitates at the bottom interface. Transport is by diffusion only (no fluid flow). We set the initial concentration to be 0, and the geometric and physical parameters of the system are listed in Table 1. The computational domain is meshed uniformly with a $1 \times 150$ grid resolution, including both fluid and solid phases.

The modeling results are compared with analytical solutions. To derive the analytical solutions, we apply Equations 2 and 3 to the one-component system and obtain the following ordinary differential equations:

$$\frac{\partial[c(H - h_1 - h_2)]}{\partial t} = -k(c - c_1^{eq}) - k(c - c_2^{eq}), \tag{21a}$$

**Table 1**
*Modeling Parameters in the Simulations*

| Modeling parameters | Value |
|---|---|
| Diffusivity ($D$, m$^2$/s) | $1 \times 10^{-9}$ |
| Kinematic viscosity ($\mu_f/\rho_f$, m$^2$/s) | $1 \times 10^{-6}$ |
| *Section* 4.1*: Diffusion-reaction system* | |
|    Domain height ($H$, μm) | 30 |
|    Initial fluid height ($h_0$, μm) | 20 |
|    Reaction rate constant ($k$, m/s) | $1 \times 10^{-8}$ |
|    Molar volume ($V$, 1/[C]) | 0.05 |
| *Section* 4.2*: Multicomponent reactive flow* | |
|    Domain height ($H$, μm) | 15 |
|    Initial fluid height ($h_0$, μm) | 10 |
|    Domain length ($L$, mm) | 3 |
|    Reaction rate constant ($k_1$, m/s) | $1 \times 10^{-8}$ |
|    Reaction rate constant ($k_{23}$, m/s/[C]) | $1 \times 10^{-8}$ |
|    Molar volume for dissolved mineral ($V_1$, 1/[C]) | 0.025 |
|    Molar volume for precipitated mineral ($V_2$, 1/[C]) | 0.1 |
| *Section* 4.3*: Realistic rock* | |
|    Domain height ($H$, μm) | 576 |
|    Domain length ($L$, μm) | 870 |
|    Reaction rate constant ($k_1$, m/s) | $1 \times 10^{-7}, 1 \times 10^{-6}, 1 \times 10^{-5}$ |
|    Reaction rate constant ($k_{23}$, m/s/[C]) | $1 \times 10^{-7}, 1 \times 10^{-6}, 1 \times 10^{-5}$ |
|    Molar volume for dissolved mineral ($V_1$, 1/[C]) | 0.025 |
|    Molar volume for precipitated mineral ($V_2$, 1/[C]) | 0.1 |

$$\frac{\partial h_1}{\partial t} = k\left(c - c_1^{eq}\right)V, \tag{21b}$$

$$\frac{\partial h_2}{\partial t} = k\left(c - c_2^{eq}\right)V, \tag{21c}$$

where $h_1(t)$ and $h_2(t)$ are the solid thicknesses at the top and bottom, respectively, and $c(t)$ is an averaged concentration in the fluid. Here we assume that diffusion is much faster than reaction, so the spatial variation of concentration is small. The equilibrium concentration at the top fluid-solid interface $c_1^{eq} = 1$, and at the bottom interface $c_2^{eq} = 0$, according to Equation 20.

The computational model in Section 3 is compared with the analytical solution of Equation 21 in Figure 4. The circles and the dashed line in Figure 4 (a), which are obtained from the proposed model and the analytical solution, represent the solid domain thickness at the top where mineral dissolution occurs. The crosses (proposed model) and the solid line (analytical solution) show the bottom solid domain thickness during mineral precipitation. We observe that at the beginning, the precipitation is slower than the dissolution because there is no solute at the initial state to trigger the precipitation reaction. Figure 4 (b) shows the averaged concentration in the fluid domain. The concentration is stabilized at 0.5 when the precipitation rate equals the dissolution rate. In Figure 4, the proposed model agrees very well with the analytical solution in predicting both the solid domain thicknesses and the concentration.

### 4.2. Model Validation Against Interface Tracking Simulations

In this section, we investigate a multicomponent dissolution-precipitation problem with fluid flow. The chemical components and the reactions are described in Equations 7–11. A two-dimensional channel is considered in which
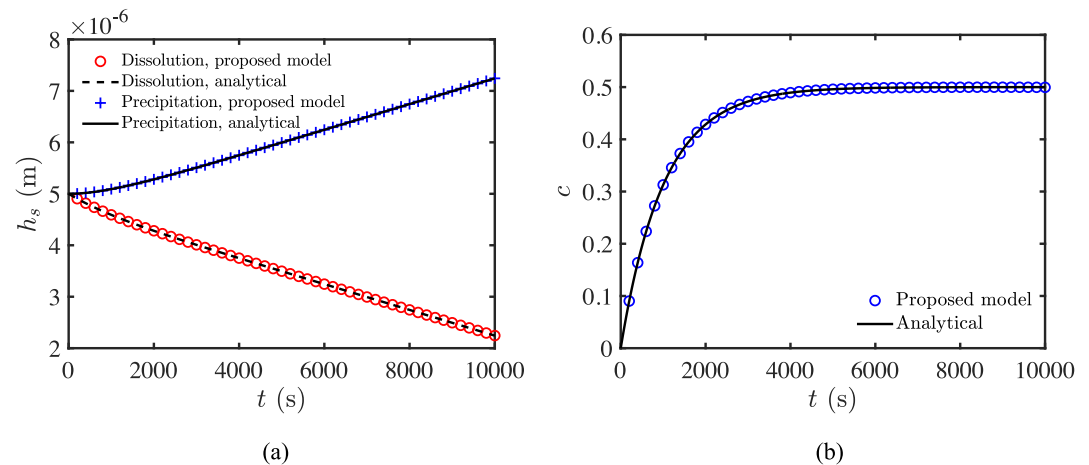
**Figure 4.** Comparison between the proposed computational model and the analytical solution: (a) thicknesses of the solid domain at the top and the bottom, where mineral dissolution and precipitation occur, respectively; (b) averaged concentration in the fluid domain.

reactive fluid is injected at the inlet and mineral dissolution-precipitation occurs on the channel walls (Figure 3b). The system is a simplified model for calcite dissolution and gypsum precipitation during acid injection in a fracture. At the inlet, fixed concentration boundary conditions ($c_1 = c_2 = 1$ and $c_3 = 0$) are applied, while zero gradient concentration boundary conditions ($\partial c_i/\partial x = 0$, $i = 1, 2, 3$) are applied at the outlet. A pressure drop $\Delta p$ is also applied between the inlet and outlet to drive fluid flow. Initially, there is no solute in the channel ($c_i$ ($t = 0$) = 0, $i = 1, 2, 3$), while the velocity field is initialized to be a parabolic steady-state profile corresponding to $\Delta p$. The geometric and physical parameters of the problem are listed in Table 1. The secondary (precipitated) mineral is selected to have a higher molar volume than the dissolving mineral, which corresponds to the case of calcite and gypsum described above. The computational domain is meshed uniformly with a $300 \times 120$ grid resolution, including both fluid and solid phases.

The multicomponent reactive flow system is solved by the computational model in Section 3. Separately, we also model the system through an interface tracking approach (Wang & Battiato, 2020, 2021), which serves as a reference solution. The interface tracking method solves the governing Equations 1–3 in the fluid domain, that is, the physical model in Section 2 is directly solved. The fluid domain is meshed by boundary-fitted grid cells and is constantly remeshed to follow the fluid-solid interface during mineral dissolution-precipitation. Since only the fluid domain is meshed, the grid resolution is $300 \times 80$, which results in an initial grid size that is the same as in our computational model.

The results obtained from the two approaches are compared. Figure 5 plots the concentration profiles along the channel centerline at = 5,000 s, where the symbols represent the proposed model and the lines represent the reference interface tracking simulation. Four pressure drop values are adopted and we employ the Péclet number to characterize the relative importance of advection versus diffusion:

$$Pe = \frac{u_0 h_0}{D} = \frac{h_0^3 \Delta p}{12 D \mu L},$$ (22)

where $u_0$ is the average fluid velocity at the initial state and $h_0$ is the initial fluid height (i.e., initial channel aperture). Here we assume all the chemical components have the same diffusivity $D$ (Table 1). In Figure 5 (a), (b) and (c), the concentration $c_1$ decreases with $x$, as the corresponding component B ($H^+$) is gradually consumed through mineral dissolution. The dissolution releases the component C ($Ca^{2+}$), so the corresponding concentration $c_3 = c(C)$ increases with $x$ near the channel inlet. Then, the component C ($Ca^{2+}$) reacts with the component E ($SO_4^{2-}$), which causes mineral precipitation. Thus, the concentration $c_2 = c(E)$ decreases with $x$, while $c_3 = c(C)$ may decrease or increase, depending on the dissolution and precipitation reaction rates. Figure 5 (d) presents an extreme case where the flow rate is very high and the solute is quickly flushed through the channel, so flat concentration profiles (no gradient) are observed.
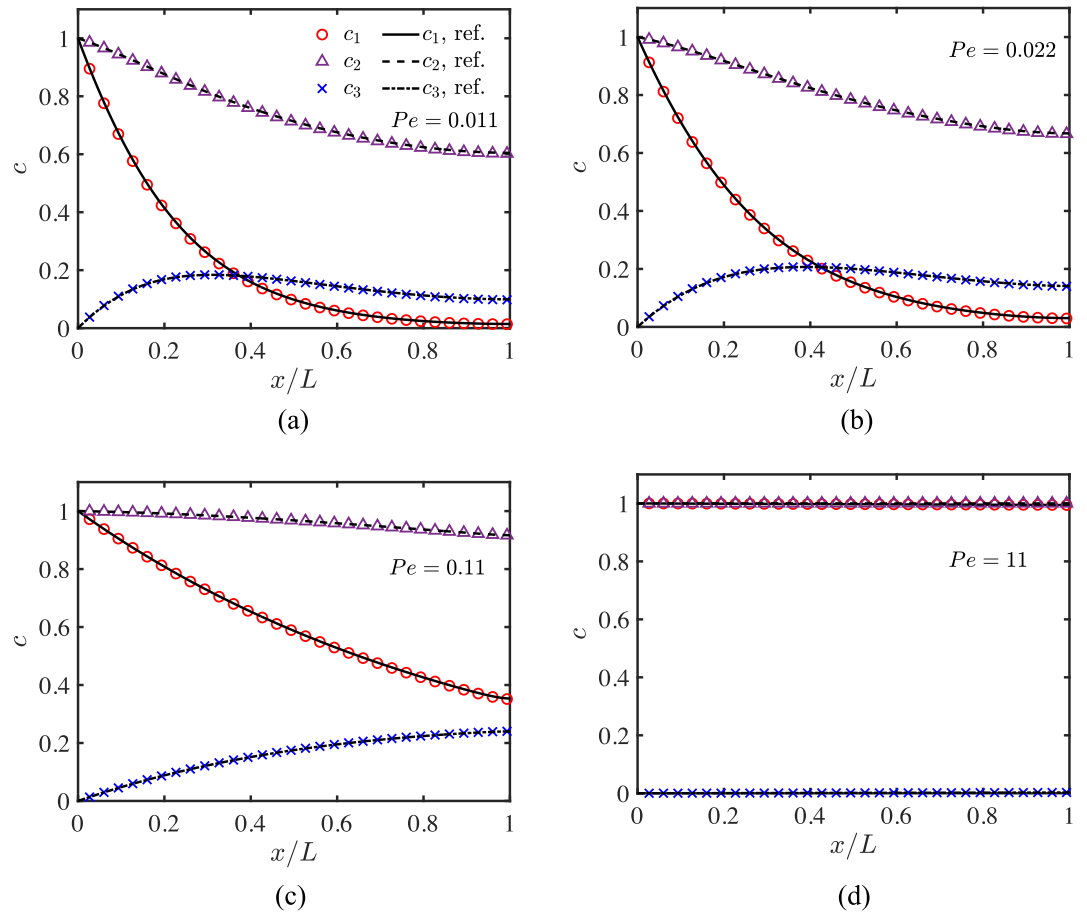
**Figure 5.** Concentration profiles, that is, $c_1 = c(B)$ $(=[H^+])$; $c_2 = c(E)$ $(=[SO_4^{2-}])$; $c_3 = c(C)$ $(=[Ca^{2+}])$, along the channel centerline at $t = 5,000$ s: (a) $Pe = 0.011$, (b) $Pe = 0.022$, (c) $Pe = 0.11$, (d) $Pe = 11$. The symbols are computed by the proposed model and the lines are results from the reference interface tracking simulation.

Figure 6 shows the channel aperture variation for the four $Pe$ values. We find dissolution is always enhanced as $Pe$ increases because more solute is injected. On the other hand, the amount of precipitated mineral increases at first, then decreases with $Pe$. This is because the precipitation reaction relies on the component C ($Ca^{2+}$), which is released through dissolution. In the low $Pe$ range, the precipitation benefits from the enhanced dissolution, as more reactant C ($Ca^{2+}$) is generated for the precipitation reaction. In the high $Pe$ range, the dissolved mineral is quickly flushed away, thus the amount of precipitation decreases.

The velocity profiles along the channel centerline at $t = 5,000$ s are plotted in Figure 7. Good agreement is observed between the model and the reference interface tracking approach for predicting concentration, channel aperture, and velocity, which indicates the accuracy of our proposed model. We also compare the proposed model with a micro-continuum method, which introduces a drag force in the momentum equation (Soulaine et al., 2017; Voller & Prakash, 1987):

$$\frac{\rho_f}{\phi}\left[\frac{\partial \mathbf{u}}{\partial t} + \nabla \cdot \left(\frac{\mathbf{uu}}{\phi}\right)\right] = \nabla p + \frac{1}{\phi}\nabla \cdot \left(\mu_f \nabla \mathbf{u}\right) - \mu_f K^{-1} u,\tag{23a}$$

$$K = K_{CK}\frac{\phi^3}{(1-\phi)^2},\tag{23b}$$

where $K_{CK}$ is an empirical parameter that controls the drag force. The selection of $K_{CK}$ affects the accuracy of the micro-continuum method. Figure 8 plots the velocity profiles across the channel at $t = 3,000$ s and $t = 5,000$ s. The
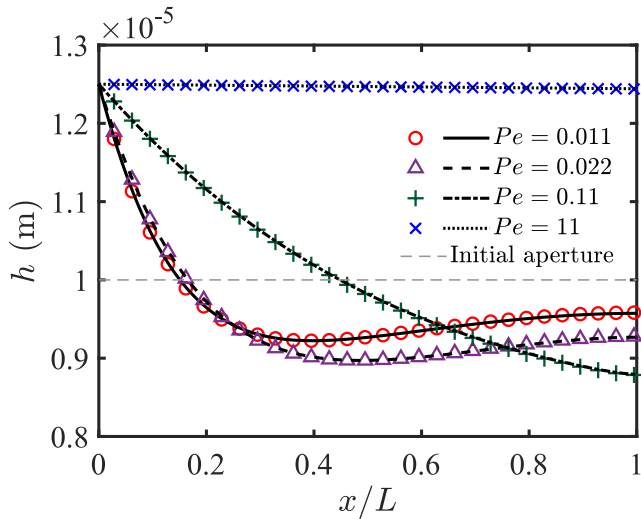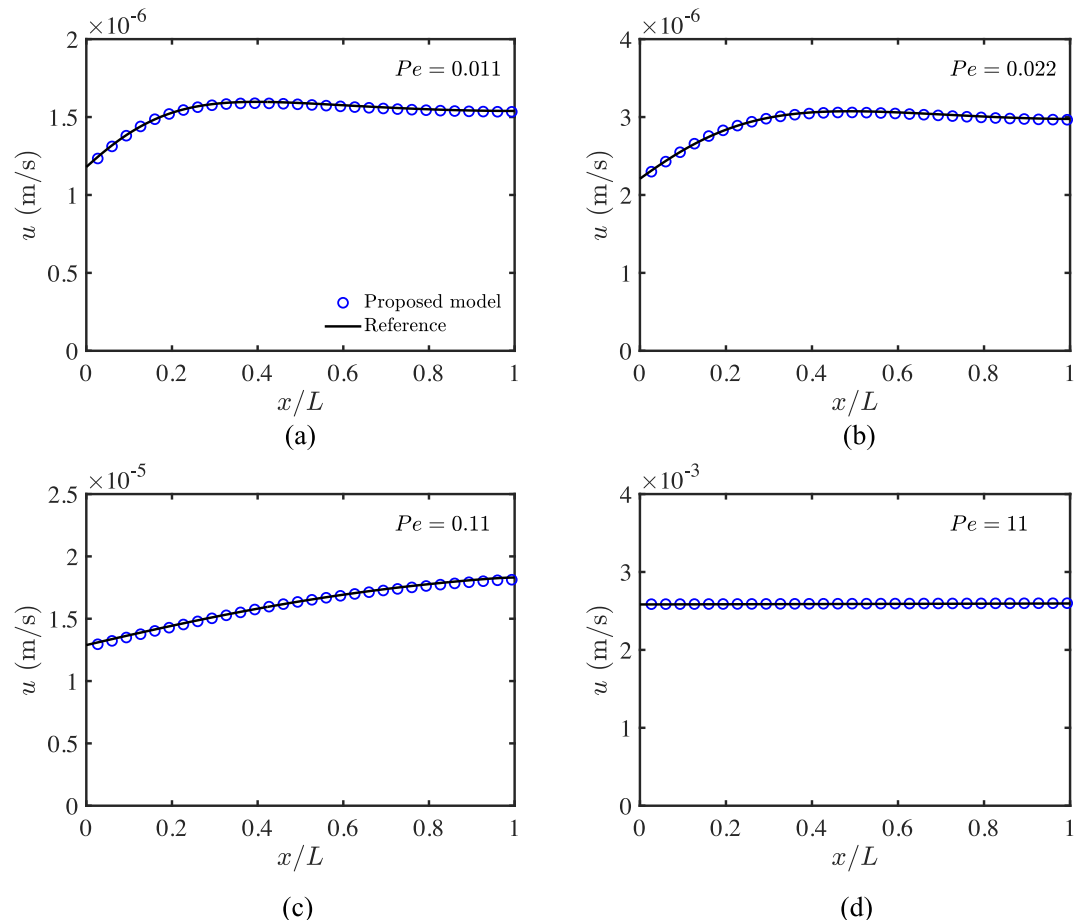
**Figure 6.** Concentration profiles along the channel centerline at $t = 5,000$ s: (a) $Pe = 0.011$, (b) $Pe = 0.022$, (c) $Pe = 0.11$, (d) $Pe = 11$. The symbols are computed using the proposed model and the lines are results from the reference interface tracking simulation.

case with $Pe = 11$ is considered as the velocity along the channel is uniform (Figure 7d). We compare the proposed model, the reference interface tracking simulation, and the micro-continuum approach. For the micro-continuum approach, the velocity decreases with $K_{CK}$, as a lower $K_{CK}$ provides a larger drag force in Equation 23. For our problem setup, the best agreement to the reference simulation is observed at $K_{CK} = 5 \times 10^{-14}$ m². On the other hand, the effective viscosity model Equation 4 compares well with the reference simulation without introducing any empirical parameters.

### 4.3. Coupled Mineral Dissolution and Precipitation in Realistic Rocks

After validation, the proposed model is used to analyze mineral dissolution-precipitation processes in more realistic pore structures. Similar to Section 4.2, we consider the multicomponent reactive system described in Equations 7–11. A pore-scale rock structure is modeled in which mineral dissolution and precipitation occur on the solid grain interfaces. We apply fixed concentration boundary conditions ($c_1 = c_2 = 1$ and $c_3 = 0$) on the left boundary of the rock structure, and zero gradient concentration boundary conditions ($\partial c_i / \partial x = 0$, $i = 1, 2, 3$) at the right boundary. Between the two boundaries, a pressure drop $\Delta p$ is applied to drive fluid flow. Initially, there is no solute in the rock ($c_i (t = 0) = 0$, $i = 1, 2, 3$), and the velocity is at the steady state corresponding to $\Delta p$ and the initial rock structure.



**Figure 7.** Velocity profiles along the channel centerline at $t = 5,000$ s: (a) $Pe = 0.011$, (b) $Pe = 0.022$, (c) $Pe = 0.11$, (d) $Pe = 11$. The circles represent the proposed model and the lines represent the reference interface tracking simulation.
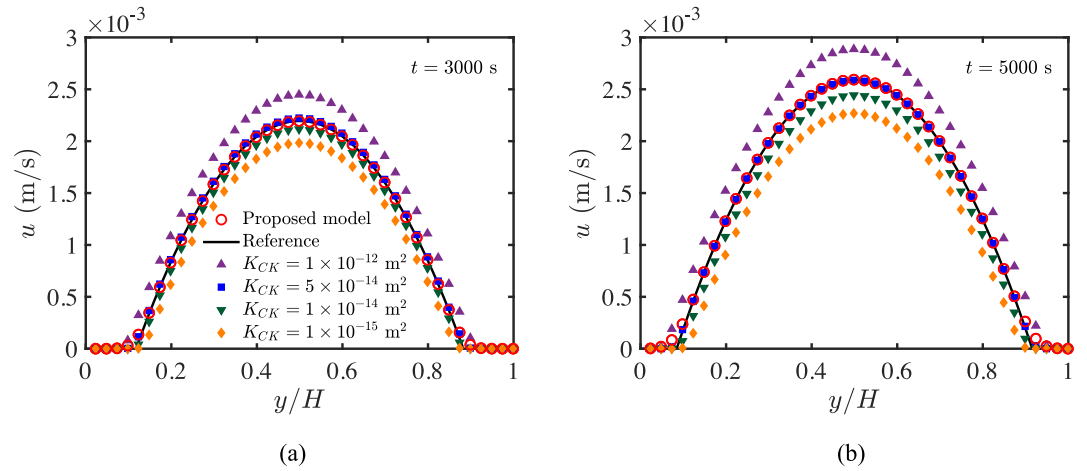
**Figure 8.** Velocity profiles across the channel with $Pe = 11$: (a) $t = 3{,}000$ s, (b) $t = 5{,}000$ s. The circles represent the proposed model and other symbols are results from the micro-continuum approach with different $K_{CK}$. The lines represent the interface tracking simulation for reference.

The rock structure is constructed based on a sandstone image (Figure 9a). The image is first binarized, and then it is smoothed by a Gauss filter to eliminate the noise in the image. Finally, the grains at the left boundary are removed to provide a clear boundary for fluid injection (Figure 9b). The geometric parameters of the structure and the physical parameters are listed in Table 1. The rock structure is meshed uniformly with a resolution $426 \times 282$, which is the same as the resolution of the processed image in Figure 9 (b). To ensure that the rock grains do not move with fluid flow, a drag term is added in Equation 4a:

$$\frac{\rho_f}{\phi}\left[\frac{\partial \mathbf{u}}{\partial t} + \nabla \cdot \left(\frac{\mathbf{uu}}{\phi}\right)\right] = \nabla p + \nabla \cdot \left(\mu_{eff}\nabla \mathbf{u}\right) - C\mathbf{u}, \tag{24a}$$

$$C = 1 \times 10^{20} \text{ s}^{-1} \text{ if } \quad \phi \in [0, 0.01], \tag{24b}$$

$$C = 0 \quad \text{if } \phi \in (0.01, 1]. \tag{24c}$$

The drag term is only applied in the solid phase where $\phi < 0.01$ to immobilize the solid grains. We note that the value of $C$ does not affect the modeling results when it is large enough, and the drag term is not necessary if the solid phase is already attached to static boundaries (e.g., in Section 4.2).

We investigate the mineral dissolution-precipitation with various flow rates and reaction rate constants. The Péclet number and two Damköhler numbers ($Da_I = Da_{II}/Pe$, Soulaine et al., 2017) are introduced to represent the relative importance of advection, diffusion, and reaction:
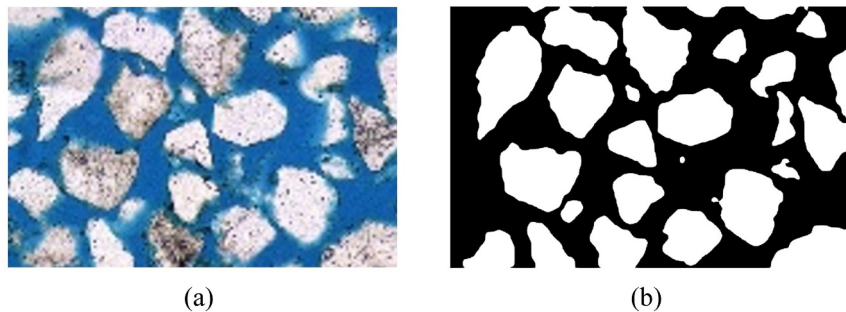


**Figure 9.** The pore-scale rock structure employed in mineral dissolution-precipitation modeling: (a) a rock thin section impregnated with epoxy, where blue represents pore space and white represents grains (image courtesy: Stanford SUPRI-A research group), (b) the image after binarization and smoothing. The image size is $870 \times 576$ μm.
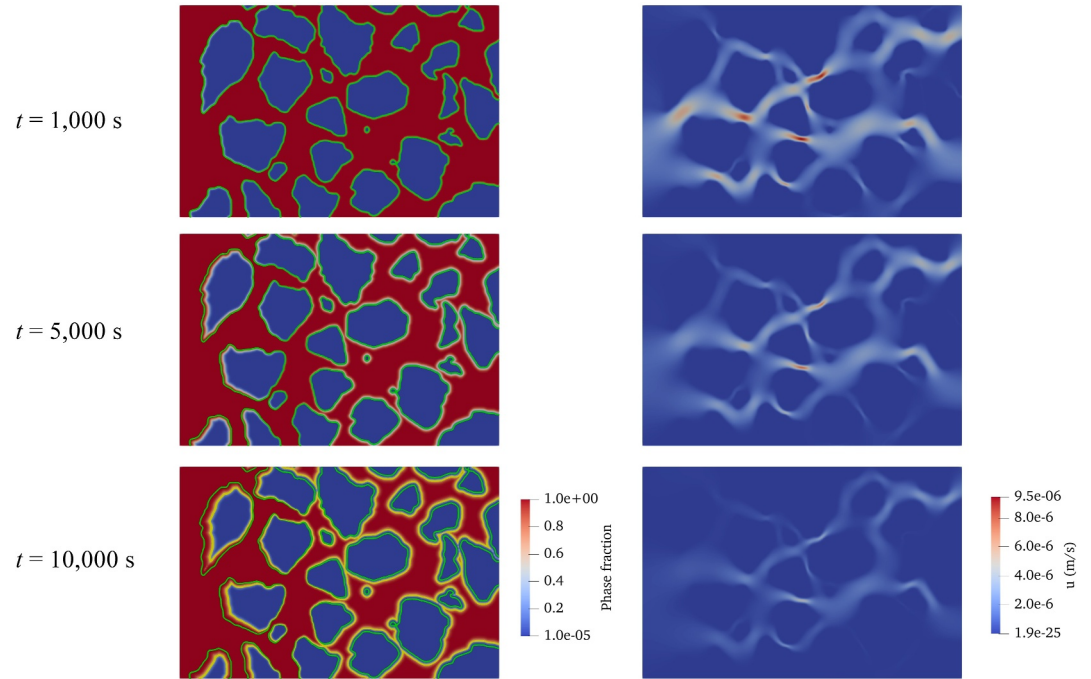
**Figure 10.** (*Regime: compact dissolution-precipitation*) The phase fraction maps (left) and the velocity fields (right) at three different times with $Pe = 2.52 \times 10^{-2}$ and $Da_{II} = 2.37 \times 10^{-3}$. The green and yellow lines in the phase fraction maps represent the initial and final grain boundaries.

$$Pe = \frac{u_0 h_0}{D}, \tag{25a}$$

$$Da_I = \frac{k_1}{u_0}, \tag{25b}$$

$$Da_{II} = \frac{k_1 h_0}{D}, \tag{25c}$$

$$u_0 = \frac{K_0 \Delta p}{\mu \phi_0 L}, \tag{25d}$$

$$h_0 = \sqrt{\frac{12 K_0}{\phi_0}}, \tag{25e}$$

Where $K_0 = 2.615 \times 10^{-11}$ m$^2$ and $\phi_0 = 0.561$ are the computed rock permeability and porosity at the initial state. Figure 10 shows the modeling results with $Pe = 2.52 \times 10^{-2}$ and $Da_{II} = 2.37 \times 10^{-3}$, where the snapshots of phase fraction fields and velocity fields are presented at three different times. We observe a compact dissolution-precipitation pattern, in which the grains near the inlet are gradually dissolved and precipitation is dominant for the grains far from the inlet. Because all the downstream flow paths are gradually clogged by the precipitation, the velocity field in the entire domain generally decreases. A different regime of dissolution-precipitation coupling is observed in Figure 11 when $Pe = 0.886$ and $Da_{II} = 2.37 \times 10^{-2}$. With the higher flow and reaction rates, mineral dissolution creates wormholes along the main flow paths, while precipitation exhibits a clustered distribution in the pore space next to the main flow paths, clogging the secondary flow paths. Thus, the velocity increases in the main flow paths, while it decreases in the secondary flow paths. Finally, we observe a third regime where dissolution is dominant over precipitation (Figure 12, with $Pe = 0.127$ and $Da_{II} = 2.37 \times 10^{-3}$). This occurs when advection is much faster than reaction (small $Da_I$), and the dissolved mineral is flushed away quickly before being able to precipitate. All the grains in the domain are gradually dissolved and the flow velocity increases as the flow paths are widened.
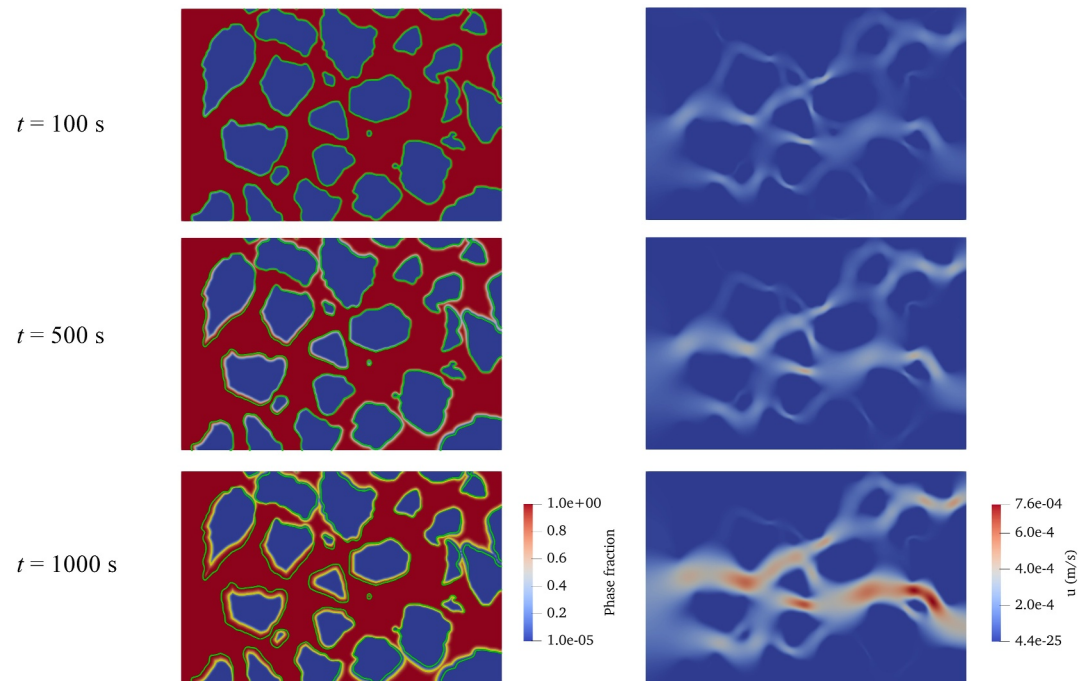
**Figure 11.** (*Regime: wormhole dissolution with clustered precipitation*) The phase fraction maps (left) and the velocity fields (right) at three different times with $Pe = 0.886$ and $Da_{II} = 2.37 \times 10^{-2}$. The green and yellow lines in the phase fraction maps represent the initial and final grain boundaries.
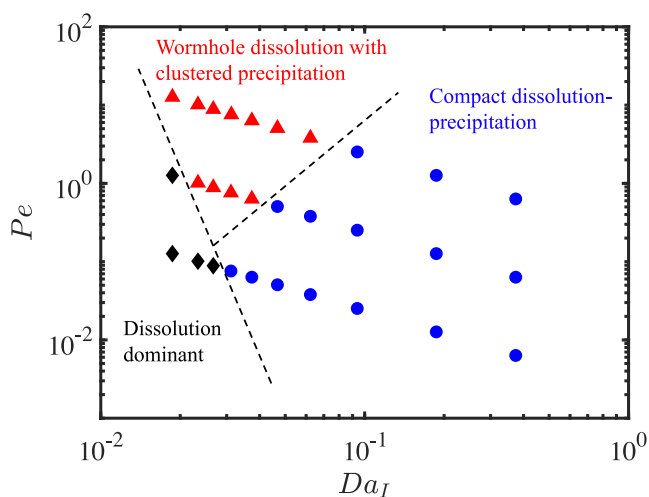
To conclude, we have identified three regimes of dissolution-precipitation coupling: (a) compact dissolution-precipitation, (b) wormhole dissolution with clustered precipitation, and (c) dissolution dominant. The three regimes are classified by $Pe$ and $Da_I$ in Figure 13. Laboratory experiments have found dissolution-precipitation patterns similar to the first and third regimes (Singurindy & Berkowitz, 2005). The second regime is observed when $0.01 < Da_I < 0.1$, which also agrees with the condition for wormhole occurrence in dissolution experiments ($0.01 < Da_I < 1$) (Fredd & Fogler, 1998; Li et al., 2019). For coupled dissolution-precipitation, the precipitation can block the main flow paths at the downstream. In such scenarios, we may observe the compact dissolution-precipitation regime rather than wormholes, for example, when $0.1 < Da_I < 1$. We also note that a precipitation dominant regime can exist when the precipitation is much faster than dissolution, that is, the dissolved ion instantaneously precipitates at the same location (Deng et al., 2022; Singurindy & Berkowitz, 2005). This is not pursued here because we assume the precipitation and dissolution have similar rates, and the scenario has been investigated in the literature (Deng et al., 2022).

The three regimes demonstrate different behavior in the permeability-porosity relationship during mineral dissolution-precipitation. We compute porosity by integrating the phase fraction field in the entire computational domain, and permeability by recording the flow rate and using Darcy's law. Both porosity and permeability are calculated at several time instances to track their variations. Figure 14 plots the permeability-porosity curves for $Da_{II} = 2.37 \times 10^{-3}$ and $Da_{II} = 2.37 \times 10^{-2}$ under various $Pe$, where all the curves begin at the initial porosity-permeability value (0.561, $2.615 \times 10^{-11}$ m$^2$). The $Pe$ and $Da_{II}$ values in Figure 14 (a) correspond to the linear distributed points at the bottom in Figure 13, which are in the "compact dissolution-precipitation" regime and the "dissolution dominant" regime. In the "compact dissolution-precipitation" regime, both porosity and permeability decrease from the initial porosity-permeability value, as the precipitation clogs all the flow paths. In the "dissolution dominant" regime, both porosity and permeability increase, since all the flow paths are widened by dissolution. The $Pe$ and $Da_{II}$ in Figure 14 (b) correspond to the linear distributed points at the middle in Figure 13, where all the three regimes exist. In the "wormhole dissolution with clustered precipitation" regime, the permeability can increase while the overall porosity decreases. The permeability increases because the main flow paths are widened by the wormhole dissolution, while the overall porosity decrease is caused by the clustered precipitation in the pore space next to the main flow paths.
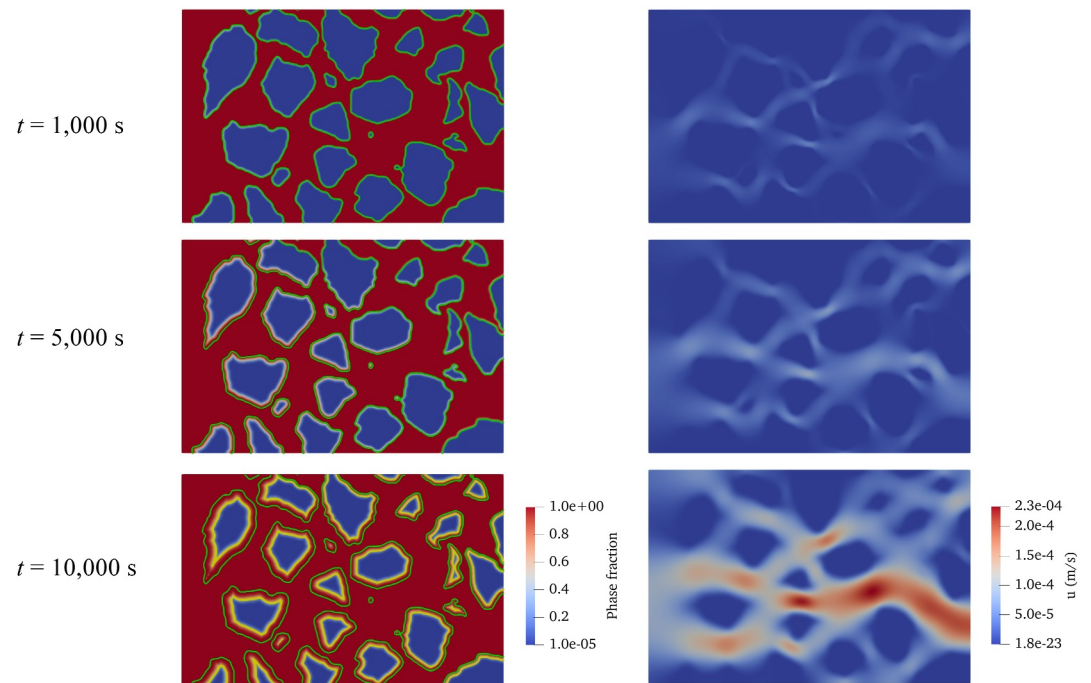
**Figure 12.** (*Regime: dissolution dominant*) The phase fraction maps (left) and the velocity fields (right) at three different times with $Pe = 0.127$ and $Da_{II} = 2.37 \times 10^{-3}$. The green and yellow lines in the phase fraction maps represent the initial and final grain boundaries.

The dissolution-precipitation regimes have not been fully conformed in laboratory experiments yet. However, Singurindy and Berkowitz ([2005](#)) have presented experiments of coupled dissolution and precipitation in fractures of carbonate rocks. Dominant dissolution at the upstream and dominant precipitation at the downstream have been observed, which is the same as the "compact dissolution-precipitation" regime. A dissolution dominant regime is also observed at high acid concentrations. The "wormhole dissolution with clustered precipitation" regime, on the other hand, cannot be observed in a single fracture. Microfluidic chips with embedded realistic rocks (Ling et al., [2022](#)) could be a promising approach for further investigation. The microfluidic devices allow accurate measurements of the moving fluid-solid interfaces, thus the dissolution dominant and precipitation dominant regions can be identified.

## 5. Conclusions

We have developed a pore-scale model for multicomponent reactive flow with coupled mineral dissolution and precipitation. A phase transformation vector field is introduced, with its direction indicating whether dissolution or precipitation occurs. Based on the phase transformation vector, the dissolution-precipitation equation is solved with the downwind differencing scheme, which ensures the phase fraction is always bounded between 0 and 1. We also employ an effective viscosity model in the momentum equation to immobilize the flow at fluid-solid interfaces, which is compared with a micro-continuum approach where an empirical parameter associated with drag forces needs to be carefully selected. Major conclusions of this work are summarized as follows.



**Figure 13.** The classification of the three regimes of dissolution-precipitation coupling, where the points represent the modeling conditions we have employed.

- A diffusion-reaction problem is investigated, where mineral dissolution and precipitation occur on two opposing fluid-solid interfaces, respectively. The proposed model achieves an excellent match with the analytical solution in predicting interface movement and concentration profiles.
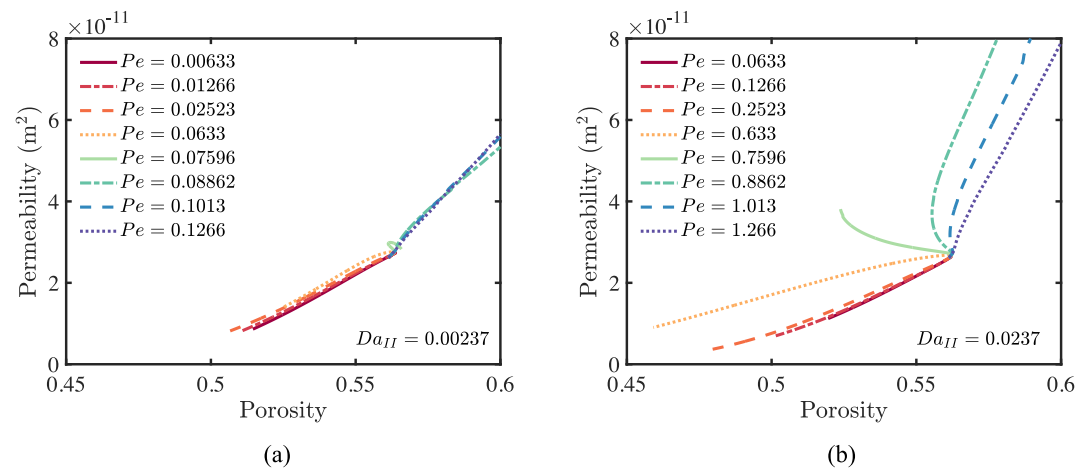
**Figure 14.** The permeability-porosity relationship during mineral dissolution-precipitation in the rock structure: (a) $Da_{II} = 2.37 \times 10^{-3}$, (b) $Da_{II} = 2.37 \times 10^{-2}$.

- Multicomponent reactive flow in a channel with mineral dissolution-precipitation is modeled by the proposed approach and an interface tracking approach for reference. The two approaches agree well in predicting concentration, interface movement, and velocity.
- The proposed model can accurately predict the parabolic velocity profile in channel flow without introducing empirical parameters. For the drag force model in the micro-continuum approach, different values of the empirical parameter $K_{CK}$ are investigated and the best match is only observed when $K_{CK} = 5 \times 10^{-14}\,\mathrm{m}^2$ with our problem setup.
- Coupled mineral dissolution and precipitation in realistic rocks is modeled and three coupling regimes are identified: (a) compact dissolution-precipitation, (b) wormhole dissolution with clustered precipitation, and (c) dissolution dominant. The three regimes exhibit different behavior in terms of the permeability-porosity relationship.

Although the rock structure investigated in this work is two dimensional, the proposed model is also applicable in three dimensional geometries. This requires more computational resources, as capturing moving interfaces generally needs higher grid resolution than flow and transport modeling. In future work, we expect to implement more sophisticated reaction models, such as the blockage effects and nucleation processes of mineral precipitation. This can help to obtain more accurate the dissolution and precipitation rates, for example, the precipitation rate can be affected by the nucleation possibilities on different mineral surfaces.

## Data Availability Statement

The data in this work is available at http://doi.org/10.5281/zenodo.10729574.

## References

Alkattan, M., Oelkers, E. H., Dandurand, J. L., & Schott, J. (1998). An experimental study of calcite and limestone dissolution rates as a function of pH from −1 to 3 and temperature from 25 to 80 C. *Chemical Geology*, *151*(1–4), 199–214. https://doi.org/10.1016/s0009-2541(98)00080-1

Borgia, A., Pruess, K., Kneafsey, T. J., Oldenburg, C. M., & Pan, L. (2012). Numerical simulation of salt precipitation in the fractures of a CO2-enhanced geothermal system. *Geothermics*, *44*, 13–22. https://doi.org/10.1016/j.geothermics.2012.06.002

Buhmann, D., & Dreybrodt, W. (1985). The kinetics of calcite dissolution and precipitation in geologically relevant situations of karst areas: 1. Open system. *Chemical Geology*, *48*(1–4), 189–211. https://doi.org/10.1016/0009-2541(85)90046-4

Burns, P. C., & Klingensmith, A. L. (2006). Uranium mineralogy and neptunium mobility. *Elements*, *2*(6), 351–356. https://doi.org/10.2113/gselements.2.6.351

Carman, P. C. (1997). Fluid flow through granular beds. *Chemical Engineering Research and Design*, *75*, S32–S48. https://doi.org/10.1016/s0263-8762(97)80003-2

Chen, L., Kang, Q., Carey, B., & Tao, W. (2014). Pore-scale study of diffusion–reaction processes involving dissolution and precipitation using the lattice Boltzmann method. *International Journal of Heat and Mass Transfer*, *75*, 483–496. https://doi.org/10.1016/j.ijheatmasstransfer.2014.03.074

Deng, H., Molins, S., Steefel, C., DePaolo, D., Voltolini, M., Yang, L., & Ajo-Franklin, J. (2016). A 2.5 D reactive transport model for fracture alteration simulation. *Environmental Science & Technology*, *50*(14), 7564–7571. https://doi.org/10.1021/acs.est.6b02184

Deng, H., Poonoosamy, J., & Molins, S. (2022). A reactive transport modeling perspective on the dynamics of interface-coupled dissolution-precipitation. *Applied Geochemistry*, *137*, 105207. https://doi.org/10.1016/j.apgeochem.2022.105207

Deng, H., Tournassat, C., Molins, S., Claret, F., & Steefel, C. I. (2021). A pore-scale investigation of mineral precipitation driven diffusivity change at the column-scale. *Water Resources Research*, *57*(5), e2020WR028483. https://doi.org/10.1029/2020wr028483

Fredd, C. N., & Fogler, H. S. (1998). Influence of transport and reaction on wormhole formation in porous media. *AIChE Journal*, *44*(9), 1933–1949. https://doi.org/10.1002/aic.690440902

Ge, Q., Yap, Y., Vargas, F., Zhang, M., & Chai, J. (2012). A total concentration method for modeling of deposition. *Numerical Heat Transfer, Part B: Fundamentals*, *61*(4), 311–328. https://doi.org/10.1080/10407790.2012.670582

Gratier, J. P., Guiguet, R., Renard, F., Jenatton, L., & Bernard, D. (2009). A pressure solution creep law for quartz from indentation experiments. *Journal of Geophysical Research*, *114*(B3). https://doi.org/10.1029/2008jb005652

Gray, F., Anabaraonye, B. U., Crawshaw, J. P., & Boek, E. S. (2021). Pore-scale dissolution mechanisms in calcite-CO2-brine systems: The impact of non-linear reaction kinetics and coupled ion transport. *Geochimica et Cosmochimica Acta*, *305*, 323–338. https://doi.org/10.1016/j.gca.2021.04.002

Gray, F., Anabaraonye, B. U., Shah, S., Boek, E. S., & Crawshaw, J. P. (2018). Chemical mechanisms of dissolution of calcite by HCl in porous media: Simulations and experiment. *Advances in Water Resources*, *121*, 369–387. https://doi.org/10.1016/j.advwatres.2018.09.007

Gray, F., & Boek, E. S. (2016). Enhancing computational precision for lattice Boltzmann schemes in porous media flows. *Computation*, *4*(1), 11. https://doi.org/10.3390/computation4010011

Gray, F., Cen, J., & Boek, E. S. (2016). Simulation of dissolution in porous media in three dimensions with lattice Boltzmann, finite-volume, and surface-rescaling methods. *Physical Review E*, *94*(4), 043320. https://doi.org/10.1103/physreve.94.043320

Hu, M., & Rutqvist, J. (2020). Finite volume modeling of coupled thermo-hydro-mechanical processes with application to brine migration in salt. *Computational Geosciences*, *24*(5), 1751–1765. https://doi.org/10.1007/s10596-020-09943-8

Huber, C., Shafei, B., & Parmigiani, A. (2014). A new pore-scale model for linear and nonlinear heterogeneous dissolution and precipitation. *Geochimica et Cosmochimica Acta*, *124*, 109–130. https://doi.org/10.1016/j.gca.2013.09.003

Jiang, M., Xu, Z., & Zhou, Z. (2021). Pore-scale investigation on reactive flow in porous media considering dissolution and precipitation by LBM. *Journal of Petroleum Science and Engineering*, *204*, 108712. https://doi.org/10.1016/j.petrol.2021.108712

Juric, D., & Tryggvason, G. (1996). A front-tracking method for dendritic solidification. *Journal of Computational Physics*, *123*(1), 127–148. https://doi.org/10.1006/jcph.1996.0011

Kampman, N., Bickle, M., Wigley, M., & Dubacq, B. (2014). Fluid flow and CO2–fluid–mineral interactions during CO2-storage in sedimentary basins. *Chemical Geology*, *369*, 22–50. https://doi.org/10.1016/j.chemgeo.2013.11.012

Kang, Q., Zhang, D., & Chen, S. (2003). Simulation of dissolution and precipitation in porous media. *Journal of Geophysical Research*, *108*(B10), 2505. https://doi.org/10.1029/2003jb002504

Li, L., Rivas, E., Gracie, R., & Dusseault, M. B. (2021). Methodology for the nonlinear coupled multi-physics simulation of mineral dissolution. *International Journal for Numerical and Analytical Methods in Geomechanics*, *45*(15), 2193–2213. https://doi.org/10.1002/nag.3262

Li, Q., Steefel, C. I., & Jun, Y. S. (2017). Incorporating nanoscale effects into a continuum-scale reactive transport model for CO2-deteriorated cement. *Environmental Science & Technology*, *51*(18), 10861–10871. https://doi.org/10.1021/acs.est.7b00594

Li, W., Einstein, H. H., & Germaine, J. T. (2019). An experimental study of matrix dissolution and wormhole formation using gypsum core flood tests: 1. Permeability evolution and wormhole geometry analysis. *Journal of Geophysical Research: Solid Earth*, *124*(11), 11055–11073. https://doi.org/10.1029/2018jb017238

Li, X., Huang, H., & Meakin, P. (2010). A three-dimensional level set simulation of coupled reactive transport and precipitation/dissolution. *International Journal of Heat and Mass Transfer*, *53*(13–14), 2908–2923. https://doi.org/10.1016/j.ijheatmasstransfer.2010.01.044

Ling, B., Sodwatana, M., Kohli, A., Ross, C. M., Jew, A., Kovscek, A. R., & Battiato, I. (2022). Probing multiscale dissolution dynamics in natural rocks through microfluidics and compositional analysis. *Proceedings of the National Academy of Sciences*, *119*(32), e2122520119. https://doi.org/10.1073/pnas.2122520119

Maher, K., Steefel, C. I., White, A. F., & Stonestrom, D. A. (2009). The role of reaction affinity and secondary minerals in regulating chemical weathering rates at the Santa Cruz Soil Chronosequence, California. *Geochimica et Cosmochimica Acta*, *73*(10), 2804–2831. https://doi.org/10.1016/j.gca.2009.01.030

Molins, S., Soulaine, C., Prasianakis, N. I., Abbasi, A., Poncet, P., Ladd, A. J., et al. (2021). Simulation of mineral dissolution at the pore scale with evolving fluid-solid interfaces: Review of approaches and benchmark problem set. *Computational Geosciences*, *25*(4), 1285–1318. https://doi.org/10.1007/s10596-019-09903-x

Oltean, C., Golfier, F., & Bues, M. A. (2013). Numerical and experimental investigation of buoyancy-driven dissolution in vertical fracture. *Journal of Geophysical Research: Solid Earth*, *118*(5), 2038–2048. https://doi.org/10.1002/jgrb.50188

Poonoosamy, J., Westerwalbesloh, C., Deissmann, G., Mahrous, M., Curti, E., Churakov, S. V., et al. (2019). A microfluidic experiment and pore scale modelling diagnostics for assessing mineral precipitation and dissolution in confined spaces. *Chemical Geology*, *528*, 119264. https://doi.org/10.1016/j.chemgeo.2019.07.039

Rabemanana, V., Vuataz, F. D., Kohl, T., & Andre, L. (2005). Simulation of mineral precipitation and dissolution in the 5-km deep enhanced geothermal reservoir at Soultz-sous-Forets, France. *Proceedings World Geothermal Congress*.

Ray, N., Oberlander, J., & Frolkovic, P. (2019). Numerical investigation of a fully coupled micro-macro model for mineral dissolution and precipitation. *Computational Geosciences*, *23*(5), 1173–1192. https://doi.org/10.1007/s10596-019-09876-x

Sabo, M. S., & Beckingham, L. E. (2021). Porosity-permeability evolution during simultaneous mineral dissolution and precipitation. *Water Resources Research*, *57*(6), e2020WR029072. https://doi.org/10.1029/2020wr029072

Singurindy, O., & Berkowitz, B. (2005). The role of fractures on coupled dissolution and precipitation patterns in carbonate rocks. *Advances in Water Resources*, *28*(5), 507–521. https://doi.org/10.1016/j.advwatres.2005.01.002

Soulaine, C., Pavuluri, S., Claret, F., & Tournassat, C. (2021). PorousMedia4Foam: Multiscale open-source platform for hydro-geochemical simulations with OpenFOAM®. *Environmental Modelling and Software*, *145*, 105199. https://doi.org/10.1016/j.envsoft.2021.105199

Soulaine, C., Roman, S., Kovscek, A., & Tchelepi, H. A. (2017). Mineral dissolution and wormholing from a pore-scale perspective. *Journal of Fluid Mechanics*, *827*, 457–483. https://doi.org/10.1017/jfm.2017.499

Soulaine, C., & Tchelepi, H. A. (2016). Micro-continuum approach for pore-scale simulation of subsurface processes. *Transport in Porous Media*, *113*(3), 431–456. https://doi.org/10.1007/s11242-016-0701-3

Starchenko, V., & Ladd, A. J. (2018). The development of wormholes in laboratory-scale fractures: Perspectives from three-dimensional simulations. *Water Resources Research*, *54*(10), 7946–7959. https://doi.org/10.1029/2018wr022948

Starchenko, V., Marra, C. J., & Ladd, A. J. (2016). Three-dimensional simulations of fracture dissolution. *Journal of Geophysical Research: Solid Earth*, *121*(9), 6421–6444. https://doi.org/10.1002/2016jb013321

Steefel, C. I., & Hu, M. (2022). Reactive transport modeling of mineral precipitation and carbon trapping in discrete fracture networks. *Water Resources Research*, *58*(9), e2022WR032321. https://doi.org/10.1029/2022wr032321

Steefel, C. I., & Lasaga, A. C. (1990). Evolution of dissolution patterns: Permeability change due to coupled flow and reaction. *Chemical Modeling of Aqueous Systems II, Chapter*, *16*, 212–225.

Steefel, C. I., Molins, S., & Trebotich, D. (2013). Pore scale processes associated with subsurface CO2 injection and sequestration. *Reviews in Mineralogy and Geochemistry*, *77*(1), 259–303. https://doi.org/10.2138/rmg.2013.77.8

Steefel, C. I., & Van Cappellen, P. (1990). A new kinetic approach to modeling water-rock interaction: The role of nucleation, precursors, and Ostwald ripening. *Geochimica et Cosmochimica Acta*, *54*(10), 2657–2677. https://doi.org/10.1016/0016-7037(90)90003-4

Steefel, C. I., & Yang, L. (2021). Secondary magnesite formation from forsterite under CO2 sequestration conditions via coupled heterogeneous nucleation and crystal growth. *Geochimica et Cosmochimica Acta*, *311*, 29–42. https://doi.org/10.1016/j.gca.2021.07.030

Voller, V. R., & Prakash, C. (1987). A fixed grid numerical modelling methodology for convection-diffusion mushy region phase-change problems. *International Journal of Heat and Mass Transfer*, *30*(8), 1709–1719. https://doi.org/10.1016/0017-9310(87)90317-6

Wang, Z., & Battiato, I. (2020). Patch-based multiscale algorithm for flow and reactive transport in fracture-microcrack systems in shales. *Water Resources Research*, *56*(2), e2019WR025960. https://doi.org/10.1029/2019wr025960

Wang, Z., & Battiato, I. (2021). Upscaling reactive transport and clogging in shale microcracks by deep learning. *Water Resources Research*, *57*(4), e2020WR029125. https://doi.org/10.1029/2020wr029125

Weller, H. G., Tabor, G., Jasak, H., & Fureby, C. (1998). A tensorial approach to computational continuum mechanics using object-oriented techniques. *Computers in Physics*, *12*(6), 620–631. https://doi.org/10.1063/1.168744

Xie, M., Mayer, K. U., Claret, F., Alt-Epping, P., Jacques, D., Steefel, C., et al. (2015). Implementation and evaluation of permeability-porosity and tortuosity-porosity relationships linked to mineral dissolution-precipitation. *Computational Geosciences*, *19*(3), 655–671. https://doi.org/10.1007/s10596-014-9458-3

Xu, R., Li, R., Ma, J., He, D., & Jiang, P. (2017). Effect of mineral dissolution/precipitation and CO2 exsolution on CO2 transport in geological carbon storage. *Accounts of Chemical Research*, *50*(9), 2056–2066. https://doi.org/10.1021/acs.accounts.6b00651

Xu, Z., Huang, H., Li, X., & Meakin, P. (2012). Phase field and level set methods for modeling solute precipitation and/or dissolution. *Computer Physics Communications*, *183*(1), 15–19. https://doi.org/10.1016/j.cpc.2011.08.005

Xu, Z., & Meakin, P. (2008). Phase-field modeling of solute precipitation and dissolution. *The Journal of Chemical Physics*, *129*(1), 014705. https://doi.org/10.1063/1.2948949

Yang, F., Stack, A. G., & Starchenko, V. (2021). Micro-continuum approach for mineral precipitation. *Scientific Reports*, *11*(1), 1–14. https://doi.org/10.1038/s41598-021-82807-y

Yasuhara, H., Marone, C., & Elsworth, D. (2005). Fault zone restrengthening and frictional healing: The role of pressure solution. *Journal of Geophysical Research*, *110*(B6). https://doi.org/10.1029/2004jb003327